ChemComm

RSC Publishing

COMMUNICATION

Synthesis of supported Ni@(RhNi-alloy) nanocomposites as an efficient catalyst towards hydrogen generation from $N_2H_4BH_3$†

Cite this: *Chem. Commun.*, 2013, **49**, 9992

Received 26th July 2013,
Accepted 4th September 2013

DOI: 10.1039/c3cc45697h

www.rsc.org/chemcomm

Changming Li, Yibo Dou, Jie Liu, Yudi Chen, Shan He, Min Wei,* David G. Evans and Xue Duan

Supported Ni@(RhNi-alloy) nanoparticles with a core–shell structure were prepared, which serve as an excellent catalyst towards hydrogen generation from $N_2H_4BH_3$.

Bimetallic alloy nanoparticles (NPs) have attracted considerable interest owing to their unique physicochemical properties and potential applications in contrast to monometallic counterparts.[1] Especially, noble metal-based alloy catalysts exhibit both remarkably enhanced catalytic performance as well as largely reduced usage of precious metals in heterogeneous catalysis.[2] It is known that catalytic reactions occur mainly at the catalyst surface, and the precious metals in the bulk phase almost provide no contribution. Therefore, many endeavors were devoted to synthesize small alloy NPs to increase the utilization efficiency of noble metals. Although great progress has been achieved (*e.g.*, RhNi,[1a,2d] PdCo,[2a] AuFe[2b] system), they still suffer from costly and toxic organic reagents, damaged activity by capping reagents, or serious self-agglomeration.[3] Recently, the development of core–shell nanostructures provides new opportunities for high utilization of noble metals in shells as well as the enhanced catalytic activity derived from the synergistic effect (*e.g.*, Ni@Ru,[1b] Au@Co,[4] Ni@Pt[5]). This inspires us to explore the idea of a new core–shell nanostructure: a transition metal core coated by a noble metal-containing alloy shell, for the purpose of achieving excellent catalytic behavior and a largely-reduced amount of noble metal. As far as we known, there is no report on the synthesis of such type of nanocomposites, and it is still a challenge by the use of conventional synthetic methods.

Hydrogen generation from a chemical hydrogen storage material (*e.g.*, hydrazine borane, $N_2H_4BH_3$, denoted as HB) is one of the most important reactions in hydrogen-based fuel cell technology, in which alloy catalysts are found to be rather effective.[2c,d,6] Previously, Xu *et al.* reported that noble metal-containing alloy catalysts are necessary to completely decompose HB with high H_2 selectivity.[7] However, the maximum utilization of noble metals is highly desired from the viewpoint of practical applications.

Layered double hydroxides (LDHs) are a class of naturally occurring and synthetic materials generally expressed by the formula $[M^{2+}_{1-x}M^{3+}_{x}(OH)_2](A^{n-})_{x/n}\cdot mH_2O$, in which M^{II} and M^{III} cations disperse in an ordered and uniform manner in brucite-like layers.[8] Recently, considerable interest has been focused on LDH materials as heterogeneous catalysts, by virtue of their versatility in chemical composition and structural architecture.[9] Specially, a topotactic transformation of LDH materials to supported metal NPs on a metal oxide substrate will occur upon calcination under reductive conditions.[10] Our previous work successfully prepared highly-dispersed Ni NPs immobilized on an Al_2O_3 matrix *via* the NiAl–LDH precursor approach.[11] In this work, we further fabricated supported Ni@(RhNi-alloy)/Al_2O_3 nanocomposites *via* a bottom-up method, which involves the following three steps as shown in Scheme S1 (ESI†): (1) preparation of supported Ni NPs on an Al_2O_3 substrate (Ni/Al_2O_3) from a hierarchical NiAl–LDH precursor; (2) chemical etching of Ni/Al_2O_3 by $RhCl_3$ solution to obtain Ni@Rh/Al_2O_3; (3) calcination of Ni@Rh/Al_2O_3 to achieve the Ni@(RhNi-alloy)/Al_2O_3 sample. The resulting Ni core–RhNi-alloy shell NPs supported on the Al_2O_3 matrix show excellent catalytic performance towards hydrogen generation from HB, taking the advantages of both bimetal synergistic effect and high utilization of noble metals located in the alloy shell.

The hierarchical NiAl–LDH precursor was synthesized by the urea decomposition method (see details in ESI†). The XRD pattern (Fig. S1A, ESI†) confirms the high purity of the LDH phase;[11] the SEM image (Fig. S1B, ESI†) displays the hierarchical LDH microsphere (~300 nm in diameter) composed of numerous frizzy nanoflakes intercrossing with each other. After reduction by H_2 at 450 °C, the resulting product Ni/Al_2O_3 inherits the original flower-like morphology (Fig. 1A). Abundant highly-dispersed small dots (particle size: 3–10 nm) were observed throughout the nanosheets using TEM (Fig. 1A, inset), which are identified as Ni NPs using XRD (Fig. S2a, ESI†). HRTEM images (Fig. S3, ESI†) display the spherical Ni NPs immobilized on the Al_2O_3 matrix with a lattice distance of 0.204 nm, corresponding to the Ni(111) crystal face. The as-synthesized clear, immobilized and highly-dispersed Ni NPs on

State Key Laboratory of Chemical Resource Engineering, Beijing University of Chemical Technology, Beijing 100029, P. R. China.
E-mail: weimin@mail.buct.edu.cn

† Electronic supplementary information (ESI) available: Detailed experimental procedures, TEM images, XRD patterns, H_2-TPR, and ^1H NMR data. See DOI: 10.1039/c3cc45697h

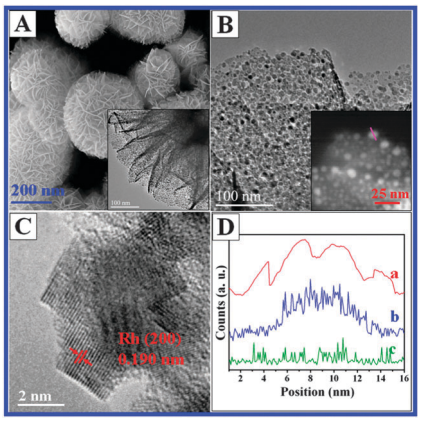

Fig. 1 Electron microscopic images of (A) SEM and TEM (inset) of Ni/Al_2O_3; (B) TEM and HAADF-STEM (inset) of $Ni@Rh/Al_2O_3$; (C) HRTEM of one single Ni@Rh NP; (D) STEM-EDS line scan profiles of a single Ni@Rh NP along the pink line in the inset of B: (a) the roughness of the Ni@Rh surface observed using a STEM-HAADF detector; (b) and (c) EDS line spectrum of Ni–K and Rh–K, respectively.

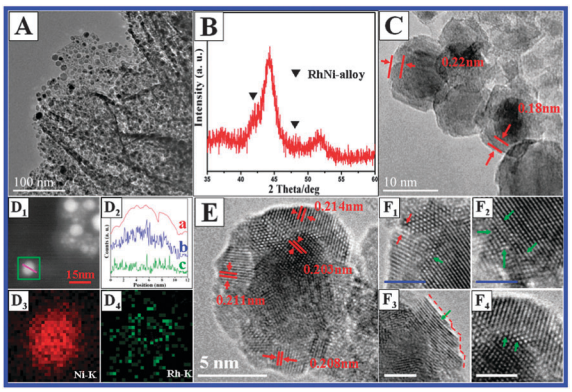

Fig. 2 Structural features of $Ni@(RhNi\text{-}alloy)/Al_2O_3$: (A) low magnification TEM; (B) XRD pattern; (C) high magnification TEM; (D_1) HAADF-STEM for a single Ni@(RhNi-alloy) NP; (D_2) the EDS line scan profiles along the pink line in D_1: (a) the surface roughness of the single Ni@(RhNi-alloy) observed using a STEM-HAADF detector; (b) and (c) EDS line spectrum of Ni–K and Rh–K, respectively; (D_3) and (D_4) EDS mapping of Ni and Rh elements of the NP; (E) HRTEM of a single Ni@(RhNi-alloy) NP, with the surface and interface structure shown in F_1–F_4 (the scale bar is 2 nm).

an Al_2O_3 matrix provide a good structural motif for the fabrication of Rh–Ni nanocomposites which is described below.

The surface-clear Ni NPs undergo a chemical etching reaction by $RhCl_3$ aqueous solution, which occurs easily and finishes within 5 min (Rh/Ni nominal ratio: 1/16; see details in the ESI†). The final Rh/Ni ratio in the product is close to 1/15 determined by elemental analysis. After etching, the integrity of the nanosheet matrix was still maintained (Fig. 1B). The XRD pattern displays the existence of both metallic Ni (2θ 44.30°, 51.61°) and Rh (2θ 40.98°) phases (Fig. S2b, ESI†). The HRTEM (Fig. 1C) reveals the typical core–shell structure of bimetal NPs, in which the cambered core and the cubic step-like shell can be recognized. According to the lattice distance of 0.190 nm, the cubic step-like shell is determined to be nanocrystalline Rh. In some cases, a whole cubic Rh shell wrapping the Ni core can also be observed (Fig. S4, ESI†). The high-angle annular dark field microscopy (HAADF-STEM) and the corresponding energy-dispersive spectroscopy (EDS) analysis were further performed to study the bimetal distribution. For the STEM-EDS line scan of a typical particle along the pink line marked in Fig. 1B-inset, four obvious convexities of the particle surface were observed (Fig. 1D, curve a), which represents the cubic step-like part of the shell revealed by the HRTEM in Fig. 1C. Although the EDS intensity of Rh is weak due to the low Rh/Ni ratio (1/15), the counts for the Rh signal increase dramatically at each convexity scope (Fig. 1D, curve c); while the Ni signal is mainly detected in the central zone (Fig. 1D, curve b). The results indicate the location of the Ni element in the centre and the Rh element at the exterior layer with non-uniformity. This further demonstrates the formation of a Ni@Rh core–shell structure after chemical etching of Ni/Al_2O_3, which agrees well with the HRTEM observation.

Supported Ni@(RhNi-alloy) NPs can be obtained after calcination in a H_2 atmosphere at 450 °C for 4 h. The TEM image (Fig. 2A) shows no obvious agglomeration, owing to the anchoring effect of the Al_2O_3 matrix.[10,11] The XRD pattern reveals the existence of a metal Ni phase (2θ 44.34°, 51.65°) accompanied with new shoulder reflections (2θ 41.85°, 48.40°) between pure metal Ni and Rh (Fig. 2B), which can be assigned to the Rh-rich alloy phase with a Rh/Ni ratio of ~3/1 estimated according to the isomorphous substitution model.[12] Compared with the XRD patterns of Ni/Al_2O_3 and $Ni@Rh/Al_2O_3$ shown in Fig. S2 (ESI†), the emergence of the RhNi alloy phase suggests the diffusing effect between the Ni core and the Rh shell in the calcination process. The high magnification TEM (Fig. 2C) demonstrates a core–shell feature with an ~6 nm core and a spherical shell of ~2 nm in thickness. From STEM and EDS analysis shown in Fig. $2D_1$–D_4, it can be observed that the surface of the calcined product becomes more smooth (Fig. $2D_2$, curve a) compared with Ni@Rh NPs, corresponding to its nearly spherical morphology. The Ni signal was also mainly detected in the central zone; however, both Ni and Rh signals were observed in the shell (Fig. $2D_2$, curves b and c). The EDS mapping for a single particle (Fig. $2D_3$–D_4) further demonstrates that the Ni element is predominantly distributed in the center while the Rh element is located in the shell. The results suggest that the observed Rh-rich alloy phase exists in the shell, and the calcined product is denoted as $Ni@(RhNi\text{-}alloy)/Al_2O_3$.

The HRTEM images further reveal the unique core–shell structure of the Ni@(RhNi-alloy) NPs. For a typical Ni@(RhNi-alloy) NP (Fig. 2E), the core is the Ni phase with a lattice distance of 0.203 nm for the Ni(111) face interval. However, the RhNi-alloy shell is not uniform; several interconnected parts with different lattice spacings (*e.g.*, 0.214, 0.211, or 0.208 nm) are identified, which can be assigned to the Rh–Ni alloy phase with variation in the Rh/Ni ratio. The results indicate the nonuniform diffusion during the transformation from the cubic step-like Rh shell to a nearly spherical RhNi-alloy shell. Most importantly, various structure defects are observed in Ni@(RhNi-alloy) NPs; for instance, the crystal boundary defect between different sections (Fig. $2F_1$, red arrow), the lattice disorder at the core–shell interface (Fig. $2F_1$, green arrow), the contraction and expansion of the lattice fringe in the shell (Fig. $2F_2$). Owing to the tension of the spherical shell, the emergence of the bending lattice (Fig. $2F_3$, green arrow) and stepped atoms (Fig. $2F_3$, red line) in the shell was detected. In some cases, the epitaxial growth of the RhNi-alloy on the Ni core was observed (Fig. $2F_4$), indicating the strong interaction between the Ni core and the RhNi-alloy shell. It is

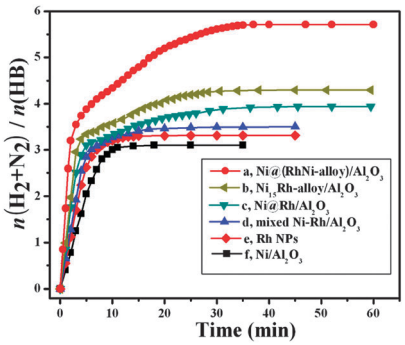

Fig. 3 Comparison of catalytic activity for hydrogen generation from HB in the presence of various catalysts: (a) Ni@(RhNi-alloy)/Al_2O_3, (b) Ni_{15}Rh-alloy/Al_2O_3, (c) Ni@Rh/Al_2O_3, (d) mixed Ni–Rh/Al_2O_3, (e) unsupported Rh NPs, (f) Ni/Al_2O_3. ([HB] = 50 mM, (Rh + Ni)/HB = 0.1, T = 50 °C).

known that the defects of metal particles play a key role in many heterogeneous catalytic processes, therefore, the observed abundant defects derived from the structural property of Ni@(RhNi-alloy) NPs may potentially contribute towards catalytic reactions.

For comparison, other Ni–Rh nanocomposites with a close Ni/Rh ratio (*e.g.*, Ni_{15}Rh-alloy/Al_2O_3, and mixed Ni–Rh/Al_2O_3) were also prepared (see details in the ESI†). The catalytic performance towards hydrogen generation from HB over the Ni@(RhNi-alloy)/Al_2O_3 catalyst was evaluated, compared with other reference samples mentioned above as well as the single Rh or Ni/Al_2O_3 NPs (Fig. 3). It can be seen that neither the single Rh nor Ni nanocatalyst can completely release the hydrogen of HB (Fig. 3e and f), while the Rh–Ni nanocomposites display better catalytic activity and selectivity (Fig. 3a–d), indicating the Rh–Ni synergistic effect for the catalytic hydrogen generation from HB. Moreover, the hydrogen generation selectivity increases in the following order: mixed Rh–Ni < Ni@Rh < Ni_{15}Rh-alloy < Ni@(RhNi-alloy). The Ni@(RhNi-alloy)/Al_2O_3 catalyst exhibits the highest hydrogen production rate with complete hydrogen generation of HB, *i.e.*, 5.74 ± 0.2 equiv. (H_2 + N_2) per HB within 40 min (Fig. 3a) at a rate of 1.2 mol H_2 per (min·mol metal). The H_2/N_2 ratio was determined to be 5.1/1.0, without any by-product (*e.g.*, NH_3) detected using GC. Moreover, this catalyst also demonstrates good reusability for five consecutive cycles by magnetic separation (Fig. S9, ESI†). TEM images further reveal that both the morphology and particle size of the catalyst after being recycled 5 times can still be maintained, indicating its good reaction stability (Fig. S10, ESI†).

As revealed by the HRTEM observations, the surfactant-free Ni@(RhNi-alloy) NPs with abundant defects provide a large number of active sites, accounting for the high activity towards HB decomposition. In addition, the grafting of Ni@(RhNi-alloy) NPs on the Al_2O_3 matrix prevents the leaching or agglomeration of NPs during the catalytic reaction, resulting in the observed good reusability and durability. The catalytic behavior is comparable to the best reported catalyst (*e.g.*, Rh_4Ni sample),[2d] but the Rh-rich alloy shell with a dramatically decreased Rh/Ni ratio (Rh/Ni = 1/15; ~60 times decrease) in Ni@(RhNi-alloy)/Al_2O_3 offers a green and cost-effective approach. The excellent catalytic performance of Ni@(RhNi-alloy)/Al_2O_3 with high utilization efficiency of noble metals demonstrated in this work makes it as a promising candidate for hydrogen generation from HB in practical applications.

In summary, well dispersed core–shell Ni@(RhNi-alloy) NPs supported on a hierarchical Al_2O_3 substrate were fabricated *via* the LDH precursor approach. The HRTEM reveals that the Ni@(RhNi-alloy) NPs possess abundant defects, with a rather thin RhNi-alloy shell (~2 nm) and a Rh/Ni ratio as low as 1/15. Compared with other Ni–Rh composite nanostructures, the Ni@(RhNi-alloy)/Al_2O_3 sample displays the best catalytic behavior towards hydrogen generation from HB decomposition with significantly improved utilization of the noble metal Rh. The surfactant-free surface and the defect-rich structure of supported Ni@(RhNi-alloy) NPs give rise to the resulting superior catalytic behavior. The strategy used with this Ni@(RhNi-alloy)/Al_2O_3 core–shell structure may open a new pathway for the design and fabrication of other noble metal-based materials in heterogeneous catalysis.

This work was supported by the 973 Program (Grant No. 2011CBA00504), the National Natural Science Foundation of China (NSFC) and the Beijing Natural Science Foundation (2132043). M. Wei particularly appreciates the financial aid from the China National Funds for Distinguished Young Scientists of the NSFC.

Notes and references

1 (*a*) H. H. Duan, D. S. Wang, Y. Kou and Y. D. Li, *Chem. Commun.*, 2013, **49**, 303; (*b*) G. Z. Chen, S. Desinan, R. Nechache, R. Rosei, F. Rosei and D. L. Ma, *Chem. Commun.*, 2011, **47**, 6308; (*c*) H. L. Jiang and Q. Xu, *J. Mater. Chem.*, 2011, **21**, 13705.
2 (*a*) D. H. Sun, V. Mazumder, Ö. Metin and S. H. Sun, *ACS Nano*, 2011, **8**, 6458; (*b*) N. Dahal and V. Chikan, *Chem. Mater.*, 2008, **20**, 6389; (*c*) J. Hannauer, O. Akdim, U. B. Demirci, C. Geanter, J.-M. Herrmann, P. Miele and Q. Xu, *Energy Environ. Sci.*, 2011, **4**, 3355; (*d*) D. C. Zhong, K. Aranishi, A. K. Singh, U. B. Demirci and Q. Xu, *Chem. Commun.*, 2012, **48**, 11945.
3 A. Roucoux, J. Schulz and H. Patin, *Chem. Rev.*, 2002, **102**, 3757.
4 J. M. Yan, X. B. Zhang, T. Akita, M. Haruta and Q. Xu, *J. Am. Chem. Soc.*, 2008, **130**, 17479.
5 X. Yang, F. Cheng, J. Liang, Z. Tao and J. Chen, *Int. J. Hydrogen Energy*, 2011, **36**, 1984.
6 (*a*) M. Yadav and Q. Xu, *Energy Environ. Sci.*, 2012, **5**, 9698; (*b*) A. Staubitz, A. P. M. Robertson and I. Manners, *Chem. Rev.*, 2010, **110**, 4079; (*c*) J. Yang, A. Sudik, C. Wolverton and D. J. Siegel, *Chem. Soc. Rev.*, 2010, **39**, 656; (*d*) D. J. Heldebrant, A. Karkamkar, N. J. Hess, M. Bowden, S. Rassat, F. Zheng, K. Rappe and T. Autrey, *Chem. Mater.*, 2008, **20**, 5332; (*e*) H. Kim, A. Karkamkar, T. Autrey, P. Chupas and T. Proffen, *J. Am. Chem. Soc.*, 2009, **131**, 13749; (*f*) G. Wolf, J. Baumann, F. Baitalow and F. P. Hoffmann, *Thermochim. Acta*, 2000, **343**, 19; (*g*) F. Baitalow, J. Baumann, G. Wolf, K. Jaenicke-Rößler and G. Leitner, *Thermochim. Acta*, 2002, **391**, 159; (*h*) H. L. Jiang and Q. Xu, *Catal. Today*, 2011, **170**, 56.
7 Ç. Ç. akanyıldırım, U. B. Demirci, T. Şxener, Q. Xu and P. Miele, *Int. J. Hydrogen Energy*, 2012, **37**, 9722.
8 (*a*) A. M. Fogg, A. L. Rohl, G. M. Parkinson and D. O'Hare, *Chem. Mater.*, 1999, **11**, 1194; (*b*) S. He, S. T. Zhang, J. Lu, Y. F. Zhao, J. Ma, M. Wei, D. G. Evans and X. Duan, *Chem. Commun.*, 2011, **47**, 10797.
9 H. C. Liu and E. Z. Min, *Green Chem.*, 2006, **8**, 657.
10 S. He, Z. An, M. Wei, D. G. Evans and X. Duan, *Chem. Commun.*, 2013, **49**, 5912.
11 S. He, C. M. Li, H. Chen, D. S. Su, B. S. Zhang, X. Z. Cao, B. Y. Wang, M. Wei, D. G. Evans and X. Duan, *Chem. Mater.*, 2013, **1**, 1040.
12 S. K. Singh and Q. Xu, *J. Am. Chem. Soc.*, 2009, **131**, 18032.

